Switching the Symmetry of Graphene Plasmons with Nanoemitters for Ultimate Infrared-Light Confinement

In-Ho Lee,[1,2] Luis Martin-Moreno,[3,4] Phaedon Avouris,[1,5] Tony Low,[1] and Sang-Hyun Oh[1,*]

[1]*Department of Electrical and Computer Engineering, University of Minnesota, Minneapolis, Minnesota, USA*

[2]*Center for Opto-Electronic Materials and Devices, Korea Institute of Science and Technology, Seoul 02792, South Korea*

[3]*Instituto de Nanociencia y Materiales de Aragón (INMA), CSIC-Universidad de Zaragoza, Zaragoza 50009, Spain*

[4]*Departamento de Física de la Materia Condensada, Universidad de Zaragoza, Zaragoza 50009, Spain*

[5]*IBM Thomas J. Watson Research Center, Yorktown Heights, New York, USA*

Vertical plasmonic coupling in double-layer graphene leads to two hybridized plasmonic modes: the optical and the acoustic plasmon with symmetric and antisymmetric charge distributions across the interlayer gap, respectively. However, in most experiments based on far-field excitation, only the optical plasmon are dominantly excited in the double-layer graphene systems. Here, we propose strategies to selectively and efficiently excite the acoustic plasmon with single or multiple nanoemitters. The analytical model developed here elucidates the role of the position and arrangement of the emitters on the symmetry of the resulting graphene plasmons. In addition, we present an optimal device structure to enable an experimental observation of the acoustic plasmon in double-layer graphene toward the ultimate level of plasmonic confinement defined by a monoatomic spacer, which is inaccessible with a graphene-on-a-mirror architecture.

I. INTRODUCTION

Various two-dimensional (2D) materials, including graphene [1–8] and black phosphorus [9–11] have emerged as promising plasmonic platforms due to their ability to confine light into deep subdiffraction volumes and modulate plasmon properties through doping. In particular, subwavelength light confinement via polaritons [12–14] in 2D materials has been a focus of intense research [15–20] since it will open up opportunities to develop advanced optoelectronic devices operating at mid-infrared frequencies, such as metasurfaces [21–23], photodetectors [24,25], and biosensors [26–29]. Furthermore, the acoustic plasmon [18,30–38], the hybridized bonding plasmon modes that are supported by spatially separated 2D materials, offers a practical route to push the light confinement toward its ultimate limit. In contrast to its counterpart with symmetric charge distributions (antibonding), the antisymmetric charge distribution of the acoustic plasmon between two 2D layers helps confine most electromagnetic energy within the interlayer gap. As a result, the plasmon confinement can be pushed to the extreme

limit, beyond that of conventional 2D plasmons, as defined by the separation between the 2D layers.

To date, the acoustic plasmon has been primarily observed in a setup involving a single layer of graphene near a metal film [18,35,36]. In this configuration, the graphene layer is paired with its image in the metal film due to the electromagnetic mirroring effect. However, since the mirror image of the real graphene has an opposite charge distribution, the graphene-metal system can only support the acoustic plasmon, and the optical plasmon becomes a dark mode. In a double-layer system, in contrast, the optical plasmon is preferably excited due to the system's symmetry, while the acoustic plasmon becomes difficult to excite [39]. Therefore, experimental observation of the acoustic plasmon in double-layer systems has been challenging.

In this work, we show how to selectively excite acoustic versus optical plasmon modes in the double-layer graphene system. First, we develop a theory to calculate plasmon excitation by single or multiple nanoemitters of deep subwavelength dimensions. Second, building upon the physical understanding facilitated by theory, we design a far-field resonator that can selectively and efficiently excite the acoustic plasmon in the graphene double-layer system, allowing us to reach the ultimate monoatomic

---

*sang@umn.edu

064039-1

layer limit of the plasmon confinement inaccessible with the graphene-on-a-mirror system.

II. MATHEMATICAL FORMULATION

Let us consider two infinite graphene sheets with a gap of g between them, as shown in Fig. 1(a). The optical conductivity of the graphene sheets, designated by σ_υ, is calculated using the local approach [8], taking into account a doping level μ of 0.4 eV, a damping rate η of 10 meV, and the temperature T of 300 K with the integer $\upsilon = 1$, 2 used to distinguish between the two graphene layers located at $z = 0$ and $z = g$. A Hertzian dipole used to excite plasmons can be located in one of three regions separated by the two graphene sheets. Here we consider the general case with three dipoles in each region, all oscillating in the x direction and with current densities of $J_{l,x}$ where $l =$ I, II, III is a region index. The positions of the dipoles are determined by $z = h_l$. The solution for a single dipole can be obtained by setting two of the three dipole magnitudes to zero. The electromagnetic fields can be decomposed in a Fourier expansion in in-plane momentum q. For each value of q, the forced wave equation for the electric fields ($E_{l,x}$) in a medium with relative permittivity ϵ_l is given as

$$\frac{\partial^2 E_{l,x}}{\partial z^2} - \gamma_l^2 E_{l,x} = \frac{i J_{l,x} \gamma_l^2}{\omega \epsilon_l \epsilon_0} \delta(z - h_l) \quad l = \text{I}, \text{II}, \text{III}, \quad (1)$$

where $\gamma_l = \sqrt{q^2 - \epsilon_l k_0^2}$ with the in-plane momentum of the plasmon q and $k_0 = 2\pi/\lambda_0$ with λ_0 being the free-space wavelength. The solutions for Eq. (1) are given as

$$E_x = \begin{cases} E_\text{I} e^{\gamma_\text{I} z} - \xi_\text{I} e^{-\gamma_\text{I}|z - h_\text{I}|}, & (z < 0) \\ E_\text{II,p} e^{-\gamma_\text{II} z} + E_\text{II,n} e^{\gamma_\text{II} z} - \xi_\text{II} e^{-\gamma_\text{II}|z - h_\text{II}|}, \\ (0 < z < g) \\ E_\text{III} e^{-\gamma_\text{III}(z - g)} - \xi_\text{III} e^{-\gamma_\text{III}|z - h_\text{III}|}, & (g < z) \end{cases} \quad (2)$$

where $\xi_l = i J_{l,x} \gamma_l / 2\omega\epsilon_l\epsilon_0$. By applying electromagnetic boundary conditions at the interfaces $z = 0$ and $z = g$, the magnitudes of the electric fields in the gap region, represented by $\mathbf{E} = \binom{E_\text{II,p}}{E_\text{II,n}}$, can be related to the system matrix, $\mathbf{M}$, and the source matrix, $\mathbf{S}$ through the equation $\mathbf{E} = \mathbf{M}^{-1}\mathbf{S}$ where

$$\mathbf{M} = \begin{bmatrix} (\Pi_1 + 1)\alpha_1 + 1 & (\Pi_1 + 1)\alpha_1 - 1 \\ (\Pi_2 + 1 - \alpha_2)e^{-\gamma_\text{II} g} & (\Pi_2 + 1 + \alpha_2)e^{\gamma_\text{II} g} \end{bmatrix}, \quad (3)$$

$$\mathbf{S} = \begin{bmatrix} -2\alpha_1\xi_\text{I} e^{-\gamma_\text{I}|h_\text{I}|} + \xi_\text{II} A e^{-\gamma_\text{II}|h_\text{II}|} \\ \xi_\text{II} B e^{-\gamma_\text{II}|g - h_\text{II}|} - 2\xi_\text{III} e^{-\gamma_\text{III}|g - h_\text{III}|} \end{bmatrix}, \quad (4)$$

where $\Pi_1 = i\sigma_1\gamma_\text{I}/\omega\epsilon_\text{I}\epsilon_0$, $\Pi_2 = i\sigma_2\gamma_\text{III}/\omega\epsilon_\text{III}\epsilon_0$, $\alpha_1 = \gamma_\text{II}\epsilon_\text{I}/\gamma_\text{I}\epsilon_\text{II}$, $\alpha_2 = \gamma_\text{III}\epsilon_\text{II}/\gamma_\text{II}\epsilon_\text{III}$, $A = (\Pi_1 + 1)\alpha_1 - 1$, and $B = \Pi_2 + 1 - \alpha_2$. The zeros for the determinant of $\mathbf{M}$ give

the plasmon dispersion of a double-layer system, which is given as

$$\frac{[(\Pi_1 + 1)\alpha_1 + 1][\Pi_2 + 1 + \alpha_2]}{[(\Pi_1 + 1)\alpha_1 - 1][\Pi_2 + 1 - \alpha_2]} = e^{-2\gamma_\text{II} g}. \quad (5)$$

Figure 1(b) shows the plasmon dispersion in a graphene double-layer with a gap size of 10 nm and $\varepsilon_\text{I} = \varepsilon_\text{II} = \varepsilon_\text{III} = 1$. The more confined mode corresponds to the acoustic plasmon, while the other is the optical plasmon. From $E_\text{II,p}$ and $E_\text{II,n}$, E_I and E_III are given as

$$E_\text{I} = E_\text{II,p} + E_\text{II,n} + \xi_\text{I} e^{-\gamma_\text{I}|h_\text{I}|} - \xi_\text{II} e^{-\gamma_\text{II}|h_\text{II}|}, \quad (6)$$

$$E_\text{III} = E_\text{II,p} e^{-\gamma_\text{II} g} + E_\text{II,n} e^{\gamma_\text{II} g} - \xi_\text{II} e^{-\gamma_\text{II}|g - h_\text{II}|}$$
$$+ \xi_\text{III} e^{-\gamma_\text{III}|g - h_\text{III}|}. \quad (7)$$

The mathematical derivation for the case of a vertically aligned dipole can be found in Appendix A. A measure of the character of the plasmons excited from a nanoemitter χ can be defined by the in-phase relative amplitude of E_x at the two graphene layers. The in-phase and out-of-phase plasmon contributions can be computed using the Fourier spectrum of E_x. For example, the Fourier spectra of E_x fields at the two graphene surfaces, i.e., $z = 0$ (upper surface) and $z = g$ (lower surface), excited with a horizontally polarized emitter at $h = 10$ nm, are shown in Fig. 1(c). The peaks at larger momenta correspond to acoustic plasmon contributions, while peaks at smaller momenta come from optical plasmon contributions. The red-colored portion of the plot shows out-of-phase components, while the blue-colored portion indicates the in-phase component, which also agrees with the symmetry of the acoustic and optical plasmon. Here, we define the measure of acoustic plasmon content χ_υ from the Fourier spectra of graphene plasmons excited with a nanoemitter as follows:

$$\chi_\upsilon := \frac{\int_{\Phi_\upsilon} |E_{\upsilon,x}| dq - \int_{\Phi_\upsilon^c} |E_{\upsilon,x}| dq}{\int_{\Phi_\upsilon} |E_{\upsilon,x}| dq + \int_{\Phi_\upsilon^c} |E_{\upsilon,x}| dq}, \quad (8)$$

where $\upsilon = 1, 2$ refers to the cases of $z = 0$ and $z = g$, respectively, and $\Phi_\upsilon = \{\phi_\upsilon | \pi/2 \leq \phi_\upsilon < 3\pi/2\}$ with ϕ_υ being the relative phase of $E_{\upsilon,x}$ to the other layer. The measure of the acoustic plasmon content for the entire system is given as $\chi = (\chi_1 + \chi_2)/2$. Note that $\chi \to 1$ when the acoustic plasmon dominates while $\chi \to -1$ when the optical plasmon dominates.

III. SINGLE NANOEMITTER EXCITATION

The symmetry of plasmons excited by a single nanoemitter depends on the nanoemitter's polarization and its relative position to the two graphene layers. When a nanoemitter is placed far away from the system, i.e., $(h \ll -g)$ or $(g \ll h)$, the optical plasmon is preferably
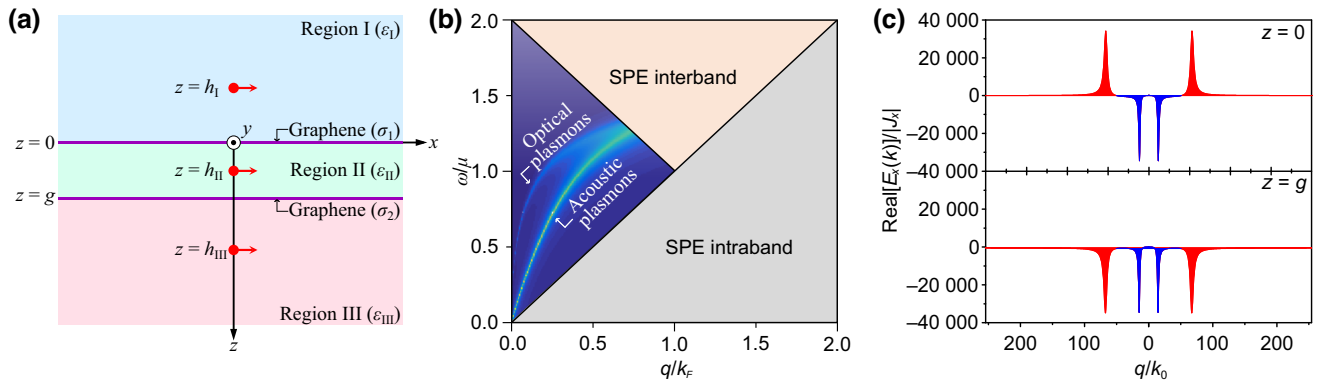
FIG. 1. Symmetry of graphene plasmons. (a) Schematic illustration of a graphene double-layer system. Three horizontally polarized Hertzian dipoles are placed in regions I, II, and III, respectively. (b) The plasmon dispersion of the double-layer system. "SPE" stands for single-particle excitation. k_F denotes the Fermi wave vector. (c) The Fourier spectra of graphene plasmons excited with a single emitter placed 10 nm away from the upper graphene layer.

excited irrespective of the polarization of an emitter since the fields radiated by an emitter reach the two graphene layers with similar magnitudes and phases [Figs. 2(a) and 2(b)]. As a nanoemitter approaches a graphene layer, the radiated fields at both layers become more asymmetric, resulting in increased excitation of acoustic plasmons. However, even when the emitter is extremely close to one of the two graphene layers, χ remains around 0.5, suggesting a significant contribution from the optical plasmon.

On the other hand, χ can be effectively tuned between ± 1 when an emitter is placed between the two graphene layers. In contrast to the horizontal polarization, where the radiated fields at the two graphene layers are in phase, a vertically polarized dipole mandates the radiated fields

at the two graphene layers to be out of phase, resulting in a value of χ close to unity. The analytical results can be verified with numerical simulations of near-field distributions for the cases where the emitter with horizontal [Fig. 2(c)] and vertical [Fig. 2(d)] polarization is placed in the middle of the two graphene layers. In this study, the numerical results are obtained through the utilization of commercial electromagnetic simulation software that operates on the finite-element method (COMSOL Multiphysics). To perform the numerical simulations, a graphene layer is modeled as a thin film having a finite thickness of 0.34 nm. The permittivities of the graphene layer are calculated by utilizing the conductivities acquired through the local approach.

IV. MULTIPLE NANOEMITTER EXCITATION

Although a single nanoemitter with vertical polarization placed between two graphene layers can exclusively excite the acoustic plasmon, implementing such a configuration is impractical due to the difficulty in embedding a nanoemitter with a precise orientation between the two layers. Here we show that multiple nanoemitters can excite the acoustic plasmon with high efficiency, irrespective of their polarizations, making them a more attractive case for practical implementations. The case of two nanoemitters provides insight into how using multiple nanoemitters can influence the character of the excited graphene plasmons. Let us examine the situation where both nanoemitters are located a few nanometers above the double-layer system. As the distance between the two nanoemitters s increases, the relative phases of the plasmons excited by the two dipoles e^{iqs} change, leading to the oscillatory behavior of χ as a function of s, as shown in Fig. 3(a). χ is maximized when the constructive interference condition $qs = 2m\pi$ is met, with m being an integer. Notice, however, that plasmon damping limits the maximum achievable values for χ.
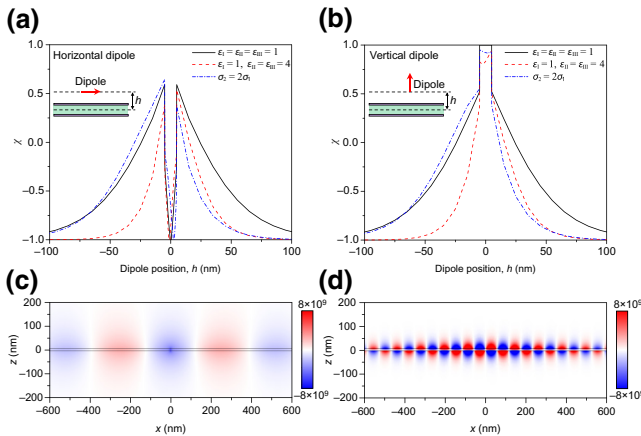

FIG. 2. Plasmon excitation with a single emitter. Measure of the acoustic plasmon content as a function of the distance from the top graphene layer of (a) horizontally and (b) vertically oriented dipole. Spatial distributions of electric fields in the x direction when $h = 0$ excited with a (c) horizontally and (d) vertically oriented dipole. In all cases, $g = 10$ nm and $\lambda_0 = 8$ μm.
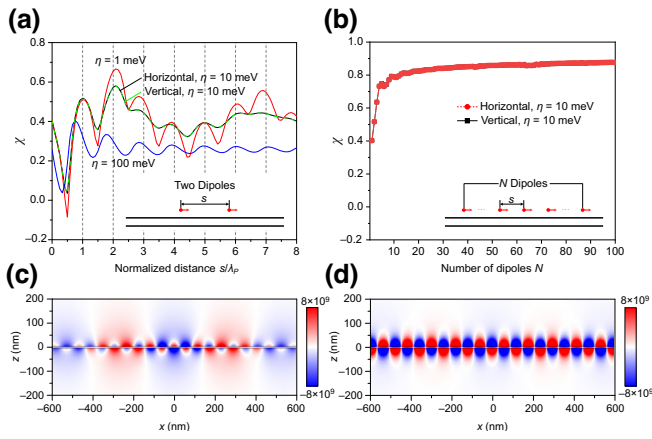
FIG. 3. Plasmon excitation with multiple emitters. (a) Measure of the acoustic plasmon content as a function of the spacing s between two dipoles. s is normalized to the wavelength of the acoustic plasmon $\lambda_P = 119$ nm. (b) Symmetry as a function of the number of dipoles. The distance between neighboring dipoles s is 119 nm. The spatial distributions of electric fields are in the x direction when (c) $N = 2$ and (d) $N = 21$. In all cases, $g = 10$ nm, $\lambda_0 = 8$ µm, and the distance of a dipole from a graphene layer is 5 nm.

Likewise, a periodic arrangement of multiple nanoemitters can reinforce the constructive interference between acoustic plasmons excited by the nanoemitters, thus increasing the acoustic contribution. The electric fields when N nanoemitters are located in the region I with a periodic spacing of s can be calculated by altering ξ_I to the expression given below.

$$\xi_I = \frac{iJ_{I,x}\gamma_I}{2\omega\epsilon_I\epsilon_0} \sum_{n=1}^{N} \exp\left[iqs\{-\frac{1}{2}(N+1)+n\}\right]. \quad (9)$$

The results shown in Fig. 3(b) demonstrate that the contribution from the acoustic plasmon indeed increases as N increases. Due to plasmon damping, however, the value of χ remains below unity even for large Ns. The results obtained from horizontal and vertical scenarios are comparable, demonstrating the robustness of the approach using multiple nanoemitters. The near-field distributions from the numerical simulations indicate that the acoustic contributions prevail for larger values of N [Figs. 3(c) and 3(d)].

V. EFFICIENT FAR-FIELD EXCITATION OF ACOUSTIC GRAPHENE PLASMONS

Motivated by the multiple-emitter approach, we suggest a resonator design that can excite the acoustic plasmon with high efficiency and selectivity. Narrow slits in a graphene layer can function as near-field emitters by scattering far-field radiation. By incorporating a periodic

arrangement of narrow slits into a graphene layer, the multiple emitters mentioned in the previous section can be effectively realized under far-field excitation. In the resonator design comprised of two identical graphene ribbon arrays, depicted in the upper panel of Fig. 4(a) (referred to as "Resonator 1"), the far-field radiation impinges on the narrow slits in the upper and lower graphene layers with similar magnitudes and phases, similar to the scenario where two identical emitters are placed on the upper and lower graphene layers. As a result, the optical plasmon is expected to be excited, while the acoustic plasmon is expected to remain in a dark mode. In contrast, the asymmetric design presented in the lower panel referred to as "Resonator 2," implements the previously discussed multiple-emitter design by incorporating a graphene ribbon layer and a continuous graphene sheet.

In Fig. 4(b), the far-field spectra numerically calculated for a photon momentum of $2\pi/p$ with a periodicity of 119 nm show that the plasmon resonances for "Resonator 1" and "Resonator 2" are located at different frequencies, indicating their distinct plasmonic characteristics. The higher-frequency resonance of "Resonator 2" is expected to originate from the acoustic plasmon since the more confined mode has higher energies for a given momentum, as shown in Fig. 1(b). To elucidate the origins of the resonances, the near-field distributions are calculated [Figs. 4(c) and 4(d)]. On the first-order resonance of
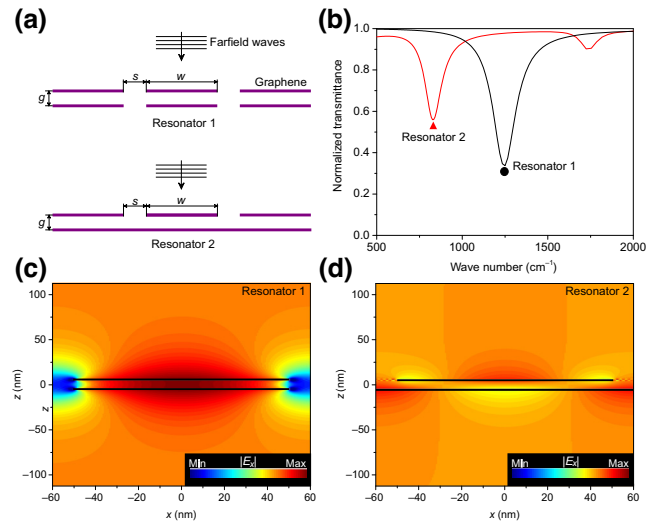

FIG. 4. Far-field excitation of the acoustic plasmon. (a) (Upper) The resonator design is based on the double graphene ribbon arrays. (Lower) The alternative resonator design uses a continuous graphene sheet with a graphene ribbon array. (b) The numerical results for the far-field spectra are obtained from the two designs. The red curve shows the case of the alternative design based on a continuous graphene layer. The spatial distributions of electric fields in the x direction for (c) the double ribbon arrays and (d) the asymmetric double-layer design. In all cases, $g = 10$, $w = 99$, and $s = 20$ nm.
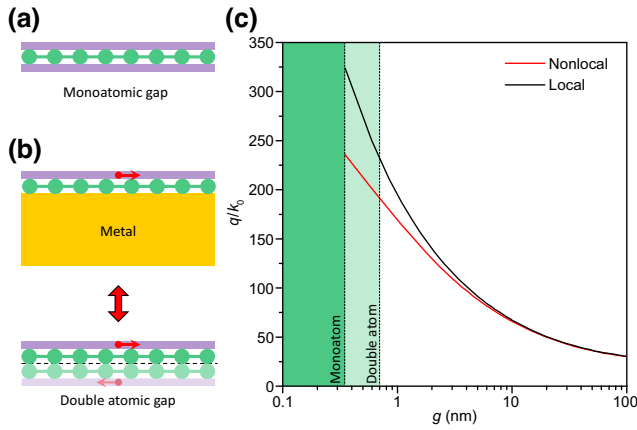
FIG. 5. Ultimate monoatomic plasmon confinement limit. (a) The schematic illustration of the double layer of graphene separated with a monoatomic layer. (b) The schematic illustration of the graphene-on-a-mirror system with a monoatomic layer spacer in between. This configuration is effectively equivalent to a double layer of graphene separated with a double-atomic-layer spacer. (c) The lateral plasmon confinement as a function of g at $\lambda_0 = 8\ \mu m$.

"Resonator 1" at a wave number of 1250 cm^{-1}, the near-field distributions (E_x) of the graphene plasmons in the upper and lower graphene layers are symmetric, indicating that the resonance originates from the optical plasmon [Fig. 4(c)]. On the first-order resonance of "Resonator 2" at a wave number of 830 cm^{-1}, the near-field distributions are asymmetric, indicating that the resonance is dominated by the acoustic plasmon [Fig. 4(d)]. The resonance at a wave number of 1750 cm^{-1} results from the second-order interference of the acoustic plasmon. The numerical results demonstrate that our resonator design effectively and selectively couples far-field radiation to the acoustic plasmon.

VI. ULTIMATE PLASMON CONFINEMENT

The excitation of the acoustic plasmon in the double-layer graphene system provides an opportunity to probe the fundamental limit of graphene plasmons. As shown in Fig. 5(a), the lateral confinement of the graphene plasmon, as measured by its effective index (q/k_0), increases with decreasing g, and the ultimate limit can be achieved with a monoatomic film, such as a monolayer of hexagonal boron nitride (h-BN) [40]. This is experimentally demonstrated in the conventional graphene-metal architecture, where a monolayer of h-BN is placed in between, as shown in Fig. 5(b). In this configuration, the interlayer separation is effectively double-atomic-layer thickness due to the electromagnetic mirroring effect. On the other hand, our double-layer graphene system can access the fundamental limit of lateral plasmon confinement at monoatomic layer thickness [Fig. 5(c)]. In practice, the achievable plasmon

confinement is limited by nonlocal effects arising from nonlocal conductivities, which can be calculated using the random-phase approximation [3] [18,41,42]. Using the asymmetric resonator design shown in Fig. 4(a) and a monolayer of h-BN as an optical spacer between the two graphene layers, we expect the far-field observation of the ultimate plasmon confinement for the double-layer graphene system will be experimentally possible.

VII. CONCLUSIONS

We demonstrate that the symmetry of the graphene plasmons can be switched with a judicious geometrical arrangement of single or multiple nanoemitters. Furthermore, our analytical theory allows us to optimize the excitation scheme to efficiently and selectively launch acoustic graphene plasmons from far-field radiation. Also, the analytical results inspired us to design an acoustic graphene plasmon resonator consisting of a continuous graphene layer and a graphene ribbon array. Our practical resonator design will enable us to experimentally observe the ultimate level of plasmon confinement defined by a monoatomic layer, inaccessible with a conventional graphene-metal coupled architecture. Also, the efficient and robust excitation of the acoustic plasmon will benefit fundamental studies such as nonlocality [43] and nonlinearity [44] as well as a variety of applications, including active metasurfaces [45], biosensors [46], and photodetectors [47].

APPENDIX A: VERTICAL DIPOLE EXCITATION

To derive the mathematical expression for surface plasmons excited by dipoles polarized along the z direction with current densities $J_{l,z}$, a similar approach as in the horizontal case can be followed. In this case, however, it is

mathematically more convenient to begin with magnetic waves. The forced wave equation for magnetic waves can be expressed as

$$\frac{\partial^2 H_{l,y}}{\partial z^2} - \gamma_l^2 H_{l,y} = -i J_{l,z} q \delta(z - h_l) \quad l = \text{I, II, III.} \quad \text{(A1)}$$

The solutions for Eq. (A1) are given as

$$
H_y = \begin{cases}
H_{\text{I}} e^{\gamma_{\text{I}} z} + \xi_{\text{I}}^{\perp} e^{-\gamma_{\text{I}} |z - h_{\text{I}}|}, & (z < 0) \\
H_{\text{II,p}} e^{-\gamma_{\text{II}} z} + H_{\text{II,n}} e^{\gamma_{\text{II}} z} + \xi_{\text{II}}^{\perp} e^{-\gamma_{\text{II}} |z - h_{\text{II}}|}, & \\
(0 < z < g) & \\
H_{\text{III}} e^{-\gamma_{\text{III}} (z - g)} + \xi_{\text{III}}^{\perp} e^{-\gamma_{\text{III}} |z - h_{\text{III}}|}, & (g < z)
\end{cases}
$$
$$\text{(A2)}$$

where $\xi_l^{\perp} = i J_{l,z} q / 2 \gamma_l$. By applying electromagnetic boundary conditions at $z = 0$ and $z = g$, the magnitudes of the magnetic field strengths in the gap region can be determined. The magnitudes represented by $\mathbf{H} = \binom{H_{\text{II,p}}}{H_{\text{II,n}}}$ can be related to the system matrix, $\mathbf{M}_{\perp}$, and the source matrix, $\mathbf{S}_{\perp}$ through the equation $\mathbf{H} = (\mathbf{M}_{\perp})^{-1} \mathbf{S}_{\perp}$ where

$$\mathbf{M}_{\perp} = \begin{bmatrix} (\Pi_1 + 1)\alpha_1 + 1 & -(\Pi_1 + 1)\alpha_1 + 1 \\ (\Pi_2 + 1 - \alpha_2)e^{-\gamma_{\text{II}} g} & -(\Pi_2 + 1 + \alpha_2)e^{\gamma_{\text{II}} g} \end{bmatrix},$$
$$\text{(A3)}$$

and

$$\mathbf{S}_{\perp} = \begin{bmatrix} 2\xi_{\text{I}}^{\perp} e^{-\gamma_{\text{I}} |h_{\text{I}}|} + \xi_{\text{II}}^{\perp} A e^{-\gamma_{\text{II}} |h_{\text{II}}|} \\ -\xi_{\text{II}}^{\perp} B e^{-\gamma_{\text{II}} |g - h_{\text{II}}|} - 2\alpha_2 \xi_{\text{III}}^{\perp} e^{-\gamma_{\text{III}} |g - h_{\text{III}}|} \end{bmatrix}, \quad \text{(A4)}$$

where $A = (\Pi_1 + 1)\alpha_1 - 1$, and $B = \Pi_2 + 1 - \alpha_2$. From $H_{\text{II,p}}$ and $H_{\text{II,n}}$, the magnitudes of magnetic fields, H_{I} and H_{III}, are given as follows:

$$H_{\text{I}} = -\alpha_1 H_{\text{II,p}} + \alpha_1 H_{\text{II,n}} + \xi_{\text{I}}^{\perp} e^{-\gamma_{\text{I}} |h_{\text{I}}|}$$
$$+ \alpha_1 \xi_{\text{II}}^{\perp} e^{-\gamma_{\text{II}} |h_{\text{II}}|}, \quad \text{(A5)}$$

$$H_{\text{III}} = \frac{1}{\alpha_2} H_{\text{II,p}} e^{-\gamma_{\text{II}} g} - \frac{1}{\alpha_2} H_{\text{II,n}} e^{\gamma_{\text{II}} g}$$
$$+ \frac{\xi_{\text{II}}^{\perp}}{\alpha_2} e^{-\gamma_{\text{II}} |g - h_{\text{II}}|} + \xi_{\text{III}}^{\perp} e^{-\gamma_{\text{III}} |g - h_{\text{III}}|}. \quad \text{(A6)}$$

Then the electric fields can be calculated by Ampére's circuital law.

APPENDIX B: PURCELL FACTOR

In this section, we determine the contributions from the acoustic plasmon by utilizing the Purcell factor and comparing our results with those shown in Fig. 2 to validate our method further. For a line of a vertical dipole located at a distance h from a graphene layer, the Purcell factor P is
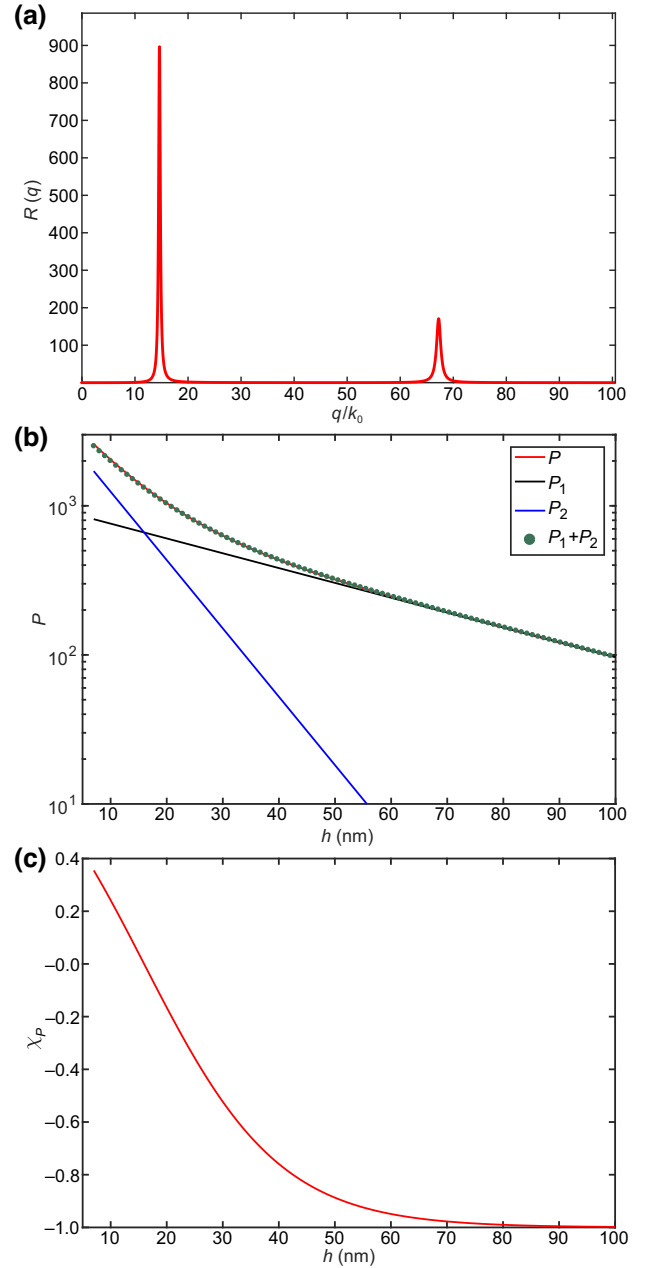

FIG. 6. Purcell factor. (a) The integrand of Eq. (A1) $R(q)$ as a function of q. (b) The spontaneous emission rates as a function of the distance between a dipole and a graphene layer (h). (c) The acoustic plasmon content, χ, as a function of h.

linked to the reflection coefficient $r(q)$ for a given in-plane momentum through the equation

$$P = 1 - 4\text{Re}\left(\int_{-\infty}^{\infty} \frac{r(q)}{4\pi k_z} e^{2ik_z z'} \frac{q^2}{k_0^2} dq \right), \quad \text{(B1)}$$

where $k_z = \sqrt{k_0^2 - q^2}$. The zeros of $r(q)$ provide the dispersion relation of graphene plasmons. The contribution of the optical and acoustic plasmon to the Purcell factor

denoted as P_1 and P_2, respectively, can be calculated by fitting the related reflection resonances to Lorentzians. As a result, the acoustic plasmon content χ_P can be expressed as $\chi_P = (P_2 - P_1)/(P_2 + P_1)$.

The calculated results are summarized in Fig. 6 for the following representative values: $\mu = 0.4$ eV, $T = 300$ K, $g = 10$ nm, and $\lambda_0 = 8$ µm. Figure 6(a) presents the integrand of Eq. (B1) denoted by $R(q)$ as a function of the in-plane momentum for the case $h = 10$ nm, which clearly reveals that nearly all of the dipole emission goes into two well-defined plasmonic modes with momenta $k_1 \approx 14.6k_0$ and $k_2 \approx 67.2k_0$. Figure 6(b) shows the total Purcell factor as a function of the distance between the emitter and one of the graphene layers. At small distances, the field emitted by the dipole couples more strongly to the more confined mode (the acoustic plasmon), but as h increases, the coupling to the acoustic plasmon decreases more rapidly than the coupling to the optical plasmon, which dominates the Purcell factor for $g \ll h$. This progression explains the dependence of χ_P on h shown in Fig. 6(c), which agrees well with the results shown in Figs. 2(a) and 2(b).

[1] Y. Zhang, Y.-W. Tan, H. L. Stormer, and P. Kim, Experimental observation of the quantum Hall effect and Berry's phase in graphene, Nature **438**, 201 (2005).

[2] A. C. Neto, F. Guinea, N. M. Peres, K. S. Novoselov, and A. K. Geim, The electronic properties of graphene, Rev. Mod. Phys. **81**, 109 (2009).

[3] E. Hwang and S. D. Sarma, Dielectric function, screening, and plasmons in two-dimensional graphene, Phys. Rev. B **75**, 205418 (2007).

[4] M. Jablan, H. Buljan, and M. Soljačić, Plasmonics in graphene at infrared frequencies, Phys. Rev. B **80**, 245435 (2009).

[5] F. H. Koppens, D. E. Chang, F. J. Garcia de Abajo, and Graphene plasmonics, A platform for strong light–matter interactions, Nano Lett. **11**, 3370 (2011).

[6] J. Chen, M. Badioli, P. Alonso-González, S. Thongrattanasiri, F. Huth, J. Osmond, M. Spasenović, A. Centeno, A. Pesquera, P. Godignon, Amaia Zurutuza Elorza, Nicolas Camara, F. Javier García de Abajo, Rainer Hillenbrand, and Frank H. L. Koppens, Optical nano-imaging of gate-tunable graphene plasmons, Nature **487**, 77 (2012).

[7] Z. Fei, A. Rodin, G. O. Andreev, W. Bao, A. McLeod, M. Wagner, L. Zhang, Z. Zhao, M. Thiemens, G. Dominguez, M. M. Fogler, A. H. Castro Neto, C. N. Lau, F. Keilmann, and D. N. Basov, Gate-tuning of graphene plasmons revealed by infrared nano-imaging, Nature **487**, 82 (2012).

[8] A. Y. Nikitin, F. Guinea, F. Garcia-Vidal, and L. Martin-Moreno, Fields radiated by a nanoemitter in a graphene sheet, Phys. Rev. B **84**, 195446 (2011).

[9] T. Low, R. Roldán, H. Wang, F. Xia, P. Avouris, L. Martin-Moreno, and F. Guinea, Plasmons and Screening in Monolayer and Multilayer Black Phosphorus, Phys. Rev. Lett. **113**, 106802 (2014).

[10] Z. Liu and K. Aydin, Localized surface plasmons in nanostructured monolayer black phosphorus, Nano Lett. **16**, 3457 (2016).

[11] I.-H. Lee, L. Martin-Moreno, D. A. Mohr, K. Khaliji, T. Low, and S.-H. Oh, Anisotropic acoustic plasmons in black phosphorus, ACS Photonics **5**, 2208 (2018).

[12] D. Basov, M. Fogler, and F. G. De Abajo, Polaritons in van der Waals materials, Science **354**, aag1992 (2016).

[13] T. Low, A. Chaves, J. D. Caldwell, A. Kumar, N. X. Fang, P. Avouris, T. F. Heinz, F. Guinea, L. Martin-Moreno, and F. Koppens, Polaritons in layered two-dimensional materials, Nat. Mater. **16**, 182 (2017).

[14] D. N. Basov, A. Asenjo-Garcia, P. J. Schuck, X. Zhu, and A. Rubio, Polariton panorama, Nanophotonics **10**, 549 (2021).

[15] V. W. Brar, M. S. Jang, M. Sherrott, J. J. Lopez, and H. A. Atwater, Highly confined tunable mid-infrared plasmonics in graphene nanoresonators, Nano Lett. **13**, 2541 (2013).

[16] A. Woessner, M. B. Lundeberg, Y. Gao, A. Principi, P. Alonso-González, M. Carrega, K. Watanabe, T. Taniguchi, G. Vignale, M. Polini, J. Hone, R. Hillenbrand, and F. H. L. Koppens, Highly confined low-loss plasmons in graphene–boron nitride heterostructures, Nat. Mater. **14**, 421 (2015).

[17] J. D. Caldwell, L. Lindsay, V. Giannini, I. Vurgaftman, T. L. Reinecke, S. A. Maier, and O. J. Glembocki, Low-loss, infrared and terahertz nanophotonics using surface phonon polaritons, Nanophotonics **4**, 44 (2015).

[18] D. A. Iranzo, S. Nanot, E. J. Dias, I. Epstein, C. Peng, D. K. Efetov, M. B. Lundeberg, R. Parret, J. Osmond, J.-Y. Hong, J. Kong, D. R. Englund, N. M. R. Peres, and F. H. L. Koppens, Probing the ultimate plasmon confinement limits with a van der Waals heterostructure, Science **360**, 291 (2018).

[19] A. Principi, E. Van Loon, M. Polini, and M. I. Katsnelson, Confining graphene plasmons to the ultimate limit, Phys. Rev. B **98**, 035427 (2018).

[20] I.-H. Lee, M. He, X. Zhang, Y. Luo, S. Liu, J. H. Edgar, K. Wang, P. Avouris, T. Low, J. D. Caldwell, and S.-H. Oh, Image polaritons in boron nitride for extreme polariton confinement with low losses, Nat. Commun. **11**, 3649 (2020).

[21] E. Carrasco, M. Tamagnone, J. R. Mosig, T. Low, and J. Perruisseau-Carrier, Gate-controlled mid-infrared light bending with aperiodic graphene nanoribbons array, Nanotechnology **26**, 134002 (2015).

[22] P. A. Huidobro, M. Kraft, S. A. Maier, and J. B. Pendry, Graphene as a tunable anisotropic or isotropic plasmonic metasurface, ACS Nano **10**, 5499 (2016).

[23] S. R. Biswas, C. E. Gutiérrez, A. Nemilentsau, I.-H. Lee, S.-H. Oh, P. Avouris, and T. Low, Tunable Graphene Metasurface Reflectarray for Cloaking, Illusion, and Focusing, Phys. Rev. Appl. **9**, 034021 (2018).

[24] M. B. Lundeberg, Y. Gao, A. Woessner, C. Tan, P. Alonso-González, K. Watanabe, T. Taniguchi, J. Hone, R. Hillenbrand, and F. H. Koppens, Thermoelectric detection and imaging of propagating graphene plasmons, Nat. Mater. **16**, 204 (2017).

[25] Q. Guo, R. Yu, C. Li, S. Yuan, B. Deng, F. J. G. de Abajo, and F. Xia, Efficient electrical detection of mid-infrared graphene plasmons at room temperature, Nat. Mater. **17**, 986 (2018).

[26] Y. Li, H. Yan, D. B. Farmer, X. Meng, W. Zhu, R. M. Osgood, T. F. Heinz, and P. Avouris, Graphene plasmon enhanced vibrational sensing of surface-adsorbed layers, Nano Lett. **14,** 1573 (2014).

[27] D. Rodrigo, O. Limaj, D. Janner, D. Etezadi, F. J. G. De Abajo, V. Pruneri, and H. Altug, Mid-infrared plasmonic biosensing with graphene, Science **349,** 165 (2015).

[28] H. Hu, X. Yang, F. Zhai, D. Hu, R. Liu, K. Liu, Z. Sun, and Q. Dai, Far-field nanoscale infrared spectroscopy of vibrational fingerprints of molecules with graphene plasmons, Nat. Commun. **7,** 12334 (2016).

[29] H. Hu, X. Yang, X. Guo, K. Khaliji, S. R. Biswas, F. J. G. de Abajo, T. Low, Z. Sun, and Q. Dai, Gas identification with graphene plasmons, Nat. Commun. **10,** 1131 (2019).

[30] E. Hwang and S. D. Sarma, Plasmon modes of spatially separated double-layer graphene, Phys. Rev. B **80,** 205405 (2009).

[31] J. Christensen, A. Manjavacas, S. Thongrattanasiri, F. H. Koppens, and F. J. García de Abajo, Graphene plasmon waveguiding and hybridization in individual and paired nanoribbons, ACS Nano **6,** 431 (2012).

[32] M. Pisarra, A. Sindona, P. Riccardi, V. M. Silkin, and J. M. Pitarke, Acoustic plasmons in extrinsic free-standing graphene, New J. Phys. **16,** 083003 (2014).

[33] T. Stauber, Plasmonics in Dirac systems: From graphene to topological insulators, J. Phys. Condens. **26,** 123201 (2014).

[34] Y. D. Glinka, S. Babakiray, T. A. Johnson, M. B. Holcomb, and D. Lederman, Nonlinear optical observation of coherent acoustic Dirac plasmons in thin-film topological insulators, Nat. Commun. **7,** 13054 (2016).

[35] P. Alonso-González, A. Y. Nikitin, Y. Gao, A. Woessner, M. B. Lundeberg, A. Principi, N. Forcellini, W. Yan, S. Vélez, A. J. Huber, K. Watanabe, T. Taniguchi, F. Casanova, L. E. Hueso, M. Polini, J. Hone, F. H. L. Koppens, and R. Hillenbrand, Acoustic terahertz graphene plasmons revealed by photocurrent nanoscopy, Nat. Nanotechnol. **12,** 31 (2017).

[36] I.-H. Lee, D. Yoo, P. Avouris, T. Low, and S.-H. Oh, Graphene acoustic plasmon resonator for ultrasensitive infrared spectroscopy, Nat. Nanotechnol. **14,** 313 (2019).

[37] I. Epstein, D. Alcaraz, Z. Huang, V.-V. Pusapati, J.-P. Hugonin, A. Kumar, X. M. Deputy, T. Khodkov, T. G. Rappoport, J.-Y. Hong, N. M. R. Peres, J. Kong, D. R. Smith, and F. H. L. Koppens, Far-field excitation of single graphene plasmon cavities with ultracompressed mode volumes, Science **368,** 1219 (2020).

[38] S. G. Menabde, I.-H. Lee, S. Lee, H. Ha, J. T. Heiden, D. Yoo, T.-T. Kim, T. Low, Y. H. Lee, S.-H. Oh, and M. S. Jang, Real-space imaging of acoustic plasmons in large-area graphene grown by chemical vapor deposition, Nat. Commun. **12,** 938 (2021).

[39] D. Rodrigo, A. Tittl, O. Limaj, F. J. G. De Abajo, V. Pruneri, and H. Altug, Double-layer graphene for enhanced tunable infrared plasmonics, Light Sci. Appl. **6,** e16277 (2017).

[40] C. R. Dean, A. F. Young, I. Meric, C. Lee, L. Wang, S. Sorgenfrei, K. Watanabe, T. Taniguchi, P. Kim, K. L. Shepard, and J. Hone, Boron nitride substrates for high-quality graphene electronics, Nat. Nanotechnol. **5,** 722 (2010).

[41] M. B. Lundeberg, Y. Gao, R. Asgari, C. Tan, B. Van Duppen, M. Autore, P. Alonso-González, A. Woessner, K. Watanabe, T. Taniguchi, R. Hillenbrand, J. Hone, M. Polini, and F. H. L. Koppens, Tuning quantum nonlocal effects in graphene plasmonics, Science **357,** 187 (2017).

[42] E. J. Dias, D. A. Iranzo, P. Gonçalves, Y. Hajati, Y. V. Bludov, A.-P. Jauho, N. A. Mortensen, F. H. Koppens, and N. Peres, Probing nonlocal effects in metals with graphene plasmons, Phys. Rev. B **97,** 245405 (2018).

[43] P. A. D. Gonçalves, T. Christensen, N. M. R. Peres, A.-P. Jauho, I. Epstein, F. H. L. Koppens, M. Soljačić, and N. A. Mortensen, Quantum surface-response of metals revealed by acoustic graphene plasmons, Nat. Commun. **12,** 3271 (2021).

[44] T. Jiang, V. Kravtsov, M. Tokman, A. Belyanin, and M. B. Raschke, Ultrafast coherent nonlinear nanooptics and nanoimaging of graphene, Nat. Nanotechnol. **14,** 838 (2019).

[45] B. Zeng, Z. Huang, A. Singh, Y. Yao, A. K. Azad, A. D. Mohite, A. J. Taylor, D. R. Smith, and H.-T. Chen, Hybrid graphene metasurfaces for high-speed mid-infrared light modulation and single-pixel imaging, Light Sci. Appl. **7,** 1 (2018).

[46] S. Chen, M. Autore, J. Li, P. Li, P. Alonso-Gonzalez, Z. Yang, L. Martin-Moreno, R. Hillenbrand, and A. Y. Nikitin, Acoustic graphene plasmon nanoresonators for field-enhanced infrared molecular spectroscopy, ACS Photonics **4,** 3089 (2017).

[47] F. Koppens, T. Mueller, P. Avouris, A. Ferrari, M. Vitiello, and M. Polini, Photodetectors based on graphene, other two-dimensional materials and hybrid systems, Nat. Nanotechnol. **9,** 780 (2014).